PHYSICAL REVIEW A **105**, 053110 (2022)

Many-electron dynamics in high-order harmonic generation of niobium: A time-dependent density-functional-theory study

Xi Chu
Department of Chemistry and Biochemistry, The University of Montana, Missoula, Montana 59812, USA

Gerrit C. Groenenboom
Institute for Molecules and Materials, Radboud University Nijmegen, Heyendaalsweg 135, NL-6525 AJ Nijmegen, The Netherlands

(Received 21 January 2022; revised 9 April 2022; accepted 26 April 2022; published 12 May 2022)

The strong-field many-electron dynamics is studied via the resonance-enhanced high-order harmonic generation (HHG) of niobium. In intense IR lights excited states of Nb with the configuration $4d^3 5s\, np$ play a vital role in the enhanced HHG below the ionization potential, even though the electron initially occupying the $5s$ orbital is the most active. The energies of these states increase linearly with the laser intensity, which causes the effective ionization potential to increase as well. Above the ionization potential, many-electron effects may cause an electronic state of Nb to be in resonance with that of Nb^+, which leads to enhanced HHG and which influences the tunneling ionization as well.

DOI: 10.1103/PhysRevA.105.053110

I. INTRODUCTION

High-order harmonic generation (HHG) not only leads to creation of ultrashort XUV pulses [1,2], it also functions as an attosecond probe [3–5]. Most studies focus on harmonic emissions with a higher photon energy than the ionization potential (I_p), whose mechanism consists of tunneling ionization, propagation of the photoelectron, and the subsequent electron rescattering in gases exposed to intense infrared lasers [6,7]. Rescattering of the electron wave packet in HHG is implemented in ultrafast imaging [8–11]. Tunneling ionization is also utilized in tracing electronic and ultrafast nuclear dynamics [12].

Mechanisms for generating harmonics with an energy lower than the I_p were described in detail recently for single-electron systems [13,14]. The resonance-enhanced emission is via instantaneous multiple rescattering. The AC Stark shift of a Rydberg state is similar to the ponderomotive energy [15], and hence can be controlled by an intense infrared (IR) light. The spatial and phase distributions of the HHG in inert gases are thus controlled via additional IR light [16,17].

Conventionally, the single active electron (SAE) approximation is adopted to study HHG. In order to generalize its application in chemistry and material science, however, a fundamental understanding of many-electron effects in HHG is required. Studies on these effects have been focused on contributions of the inner valence orbitals [18,19]. Different orbitals lead to different spatial orientation effects, which are utilized in imaging and interferometry to advance attosecond technology [9,20,21]. Time-dependent density-functional-theory (TDDFT) calculations show that resonances with the cation excited states of N_2 enhance harmonics higher than the I_p [22].

Thus, resonances may enhance harmonic emissions that are both lower and higher than the I_p. The former is subject to much larger AC Stark shifts in intense IR light than the latter. The latter involve both the cation and the electron, and hence cannot be described by the SAE approximation. To the best of our knowledge, resonance-enhanced HHG is rarely studied for harmonics both below and above the I_p. The difficulty lies in accurately describing the shifted Rydberg states in the context of many-electron dynamics.

Many-electron effects are particularly prominent in tunneling ionization of transition-metal species [23], causing substantially suppressed ionization in neutral atoms and enhanced ionization in cations relative to predictions of the SAE picture [24]. The suppression in neutral niobium is conspicuous and could reach the equivalence of increasing the I_p by a few eVs in 1500-nm lasers. This is consistent with the theory that high Rydberg states, together with the ionization threshold, move up in strong fields and the shift should be approximately the ponderomotive energy, which increases linearly with the laser intensity. Measured ionization yields [23], however, suggest that the apparent I_p ceases to increase above a certain intensity. Shifts of the I_p affect the HHG spectra as well, which will help us further understand the many-electron dynamics of transition-metal atoms.

Of a nth row transition-metal element, electrons initially occupying both the ns and the $(n-1)d$ orbitals are active in a light field. The $(n-1)d$ subshell is usually the last to fill, i.e., it is the highest occupied orbital. It is known to give rise to compounds of various oxidation states due to the low energy gap. In these compounds, the $d-d$ electron transition or ligand to metal charge transfer produces color. Meanwhile, it is the ns orbital, the second highest, that loses an electron in ionization. The electron configuration of the ground state of niobium is $a\ {}^6D_{1/2}$ $(4d^4 5s)$. The highest occupied orbital is $4d$. Without any ligands, even though the $4d$ orbitals are nearly degenerate, the $4d \rightarrow 5p$ transition spans a range of energies due to the difference in total angular momentum. The ground state of Nb$^+$ is $^5D_0$ ($4d^4$).

A TDDFT method with an optimized effective potential formalism was developed for studying the tunneling ionization of vanadium [19,25] and nickel [26]. In the TDDFT analysis, the ionization suppression of the neutral atoms and the enhancement of the cations were explained in terms of the AC Stark shifts, elevated tunneling barrier, exchange blockade, and the large centrifugal barrier for the d orbitals [26]. Here, we further examine the effects on HHG in IR fields. We focus in particular on the resonance-enhanced emissions both below and above the I_p. The AC Stark shifts and the shifts of the ionization threshold are examined together with the electronic structure of both Nb and Nb$^+$ to understand the strong-field many-electron dynamics of transition-metal elements, and hence expand the scope of attosecond chemistry.

II. METHOD

We adopt the TDDFT method developed for transition-metal atoms in intense laser fields, which employs an optimized effective potential (OEP) formalism and a spin-restricted treatment [26]. The time-dependent Kohn-Sham (KS) equation is

$$i\hbar\frac{\partial}{\partial t}\psi_{j\sigma}(\boldsymbol{r},t) = \left[\hat{H}^{(0)}_{\sigma}(\boldsymbol{r}) + \Delta v_{\sigma}(\boldsymbol{r},t) - \boldsymbol{E}(t)\cdot\boldsymbol{r}\right]\psi_{j\sigma}(\boldsymbol{r},t), \tag{1}$$

where $\sigma = \alpha$ or β is the spin index, j is orbital index, $\boldsymbol{r}$ is the spacial coordinate, t is time, $\hat{H}^{(0)}$ is the field free Hamiltonian, $\boldsymbol{E}$ is the electric field of the laser, and Δv_σ is the induced potential.

The polarization is along the z axis and

$$E(t) = f(t)\sin\omega_0 t, \tag{2}$$

where ω_0 is the angular frequency of the incident light and $f(t)$ is the field strength. We study the HHG for $f(t) = F$ ($t \geqslant$ 10 optical cycles), which matches the focus intensity. The field is gradually turned on and the field strength reaches F in 10 optical cycles:

$$f(t) = F\sin^2\frac{\omega_0 t}{40}, \quad t < \frac{20\pi}{\omega_0}. \tag{3}$$

The time-dependent 41-electron wave function of niobium is

$$\Psi(\boldsymbol{r},t) = \frac{1}{\sqrt{41!}}\det\left[\psi_{1\sigma_1}\psi_{2\sigma_2}\ldots\psi_{41\sigma_{41}}\right]. \tag{4}$$

Initially, both the external field and the induced potential are zero. We determine the initial state by solving the static KS equation with the OEP formalism described in [19]. The initial wave function is a Slater determinant of occupied orbitals corresponding to the ground-state electron configuration [Kr]$4d^4(^5D)5s$. A high-spin state is chosen to ensure representability by a single determinant.

The set of occupied spin orbitals is subsequently evolved by solving Eq. (1) with a generalized pseudospectral method [26,27]. An absorbing boundary is placed at a radial distance of $r = 400\,a_0$. The maximum distance is $1000\,a_0$. We use 400 unevenly distributed radial grid points that are denser at the nuclear center. The orbital angular momentum quantum numbers $l = 0$–12 are included. We adopt a split-operator method to propagate the time-dependent orbitals, which are transformed between the representations of the spatial grid and Hilbert space defined by the field-free Hamiltonian. The time step is 0.1 atomic units (2.419 attoseconds). Fourier transform of the induced dipole moments is converged to the 10th decimal place at the odd harmonics of the incident light with respect to all the parameters mentioned above.

The time-dependent electron density is obtained as

$$\rho(\boldsymbol{r},t) = \sum_{\sigma=\alpha}^{\beta}\sum_{i=1}^{N_\sigma}\psi^*_{i\sigma}(\boldsymbol{r},t)\psi_{i\sigma}(\boldsymbol{r},t). \tag{5}$$

In this calculation $N_\alpha = 23$ and $N_\beta = 18$.

The transient dipole moment is calculated as

$$d(t) = \iiint \rho(\boldsymbol{r},t)z\,d^3\mathbf{r}, \tag{6}$$

the Fourier transform of which is

$$d(\omega) = \frac{1}{t_f - t_i}\int_{t_i}^{t_f} d(t)e^{-i\omega t}\,dt. \tag{7}$$

We plot the HHG spectra as $|d(\omega)|^2$.

III. RESULTS AND DISCUSSION

The a^6D electronic ground state of Nb has electron configuration $4d^4(^5D)5s$. In Table I, the first four entries are electronic states that arise from exciting an electron from a $4d$ orbital to a $5p$ orbital, resulting in a $4d^35s5p$ configuration, and the last two entries correspond to the $5s \rightarrow 5p$ excitation, which gives a $4d^45p$ configuration. Column three gives the experimental excitation energies [28], where we averaged over the fine-structure states in order to remove the spin-orbit interaction, since this is not taken into account in the TDDFT calculations. In our TDDFT method, the initial state is represented by a single high-spin Slater determinant. We estimate the contribution of individual orbital excitations to a state by representing the states as Clebsch-Gordan-coupled Slater determinants. Since there are only high-spin determinants, we can represent the $4d^3$ configuration by two holes, so, e.g., we have

$$|3d^35s(^5F);M_F\rangle = \sum_{m_1m_2}|4d_{-m_1}4d_{-m_2}5s\rangle\langle 2m_12m_2|3M_F\rangle, \tag{8}$$

and subsequently the z^6G^o state is given by

$$|4d^35s(^5F)z^6G^o\rangle = \sum_{M_F,m}|4d^35s(^5F);M_F\rangle|5p_m\rangle\langle 3M_F1m|4M_G\rangle, \tag{9}$$

where the $\langle\ldots|\ldots\rangle$ are Clebsch-Gordan coefficients [29] and M_F and M_G are total orbital angular momentum projection quantum numbers. The initial state is represented by $|4d_{-1}4d_04d_14d_25s\rangle$ with orbital angular momentum projection quantum number $M_L = 2$. Because there is axial symmetry and we neglect spin-orbit coupling, we must also have $M_G = 2$. In Eq. (8) we denote a hole in orbital $4d_{m_1}$ by

TABLE I. Calculated orbital energy differences ($\Delta\epsilon$) in eV of Nb compared to the measured excitation energies from Ref. [28]. The contributions are given in % of the dominant one-electron excitation relative the ground-state configuration with $M_L = 2$.

Level	Configuration	Energy	Orbital excitation	Contribution	$\Delta\epsilon$
$z^6G^\circ_{13/2}$	$4d^35s(^5F)5p$	2.172	$4d_0 \rightarrow 5p_0$	43%	2.580
			$4d_{\pm1} \rightarrow 5p_{\pm1}$	36%	2.711
			$4d_{-1,0} \rightarrow 4d_{-2}, 5p_1$	21%	2.339
$z^6F^\circ_{11/2}$	$4d^35s(^5F)5p$	2.416	$4d_{\pm1} \rightarrow 5p_{\pm1}$	50%	2.711
			$4d_0 \rightarrow 5p_0$	33%	2.580
			$4d_{-1,0} \rightarrow 4d_{-2}, 5p_1$	17%	2.339
$z^6D^\circ_{9/2}$	$4d^35s(^5F)5p$	2.435	$4d_{\pm1} \rightarrow 5p_{\pm1}$	74%	2.711
			$4d_0 \rightarrow 5p_0$	24%	2.580
			$4d_{-1,0} \rightarrow 4d_{-2}, 5p_1$	2%	2.339
$y^6D^\circ_{9/2}$	$4d^35s(^5P)5p$	3.241	$4d_{-1,0} \rightarrow 4d_{-2}, 5p_1$	60%	2.339
			$4d_1 \rightarrow 5p_1$	40%	2.711
Average		**2.566**	$4d \rightarrow 5p$		**2.585**
$y^6F^\circ_{11/2}$	$4d^4(^5D)5p$	3.019	$4d_{-1}, 5s \rightarrow 4d_{-2}, 5p_1$	67%	2.961
			$5s \rightarrow 5p_0$	33%	3.203
$x^6D^\circ_{9/2}$	$4d^4(^5D)5p$	3.314	$5s \rightarrow 5p_0$	67%	3.203
			$4d_{-1}, 5s \rightarrow 4d_{-2}, 5p_1$	33%	2.961
Average		**3.167**	$5s \rightarrow 5p$		**3.082**

$4d_{-m_1}$, since it contributes $-m_1\hbar$ to the orbital angular momentum projection. With these two equations, the contribution of, e.g., the $4d_1 \rightarrow 5p_1$ orbital excitation is computed as

$$p(4d_1 \rightarrow 5p_1) = 2|\langle 2, -1; 2, 2|3, 1\rangle\langle 3, 1; 1, 1|4, 2\rangle|^2. \quad (10)$$

The factor of two arises because interchanging m_1 and m_2 in Eq. (8) gives the same contribution. Note that we cannot have $m_1 = m_2$, because these quantum numbers describe the holes in a high-spin $4d^3$ determinant.

The orbital energy differences in the last column of Table I are from our initial state calculation. The orbital energies are ordered as

$$\epsilon_{4d_0} > \epsilon_{4d_1} = \epsilon_{4d_{-1}} > \epsilon_{4d_2} = \epsilon_{4d_{-2}} > \epsilon_{5s}. \quad (11)$$

The highest occupied orbital is $4d_0$. In comparison, $4d_{\pm1}$ are lower by 0.127 eV, $4d_{\pm2}$ are lower by 0.372 eV, and $5s$ is lower by 0.623 eV.

Figure 1 shows the time-dependent dipole moment, which is labeled as total, of niobium in a pulsed 1500-nm laser with the intensity of 10^{13} W/cm^2. We also plot $d_{i\alpha}(t)$ for the orbitals that are initially $5s$, $4d_0$, and $4d_1$. The following comparison is demonstrated for the contributions of the orbitals:

$$d_{5s} > d_{4d_0} > d_{4d_1} (= d_{4d_{-1}}). \quad (12)$$

The $4d_2$ orbital is initially unoccupied and the magnitude of d_{4d_2} is too small to show up in the scale used in the figure. The contributions from the other $4d$ orbitals are noticeable.

Even though the $5s$ orbital is lower than the $4d$ orbitals by 0.6 eV, it contributes the most to the induced dipole because it does not have a centrifugal barrier. This is consistent with the observation that the ground-state electron configuration for the cation Nb$^+$ is $4d^4$, which is a result of electron removal from a $5s$ orbital, rather than from a $4d$ orbital. The corresponding HHG spectrum is plotted in Fig. 2 (the black solid line). The Keldysh parameter is 1.3, which means the process is not considered tunneling dominant. The measured ionization potential (I_P) of 6.76 eV is shown by the vertical red dotted line. Below the I_P, a linear decay with respect to the harmonic order is expected in a power spectrum. However, both the fifth harmonic (H5) at 4.13 eV and H7 at 5.78 eV appear higher, which we attribute to five-photon resonances involving the excited states with the configuration $4d^35s5p$. The photon energy of H5 is higher than the excitation energies in Table I because of the AC Stark shifts: The ground state is lowered slightly in the field, whereas the excited state is shifted up substantially by an amount up to the value of the ponderomotive energy, 2.10 eV.

To verify this interpretation, we change the laser wavelength to 1353 nm, while keeping other parameters the same, and obtain another HHG power spectrum of niobium as a comparison. In this case the Keldysh parameter is 1.4 and the ponderomotive energy is 1.71 eV. We show the peaks of

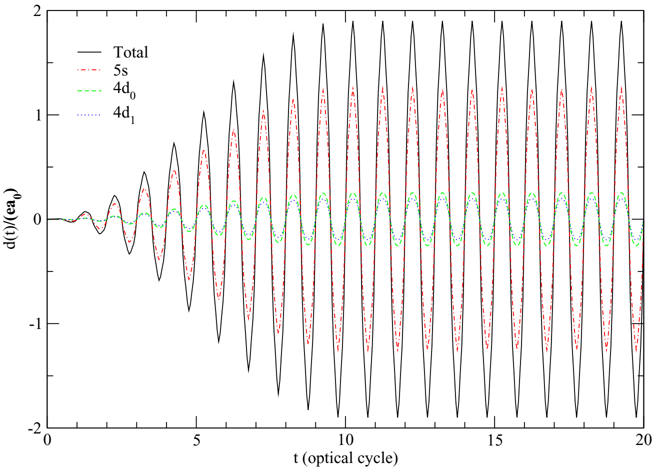

FIG. 1. Orbital contributions to the induced dipole moment of a Nb atom in a linearly polarized 1500-nm laser field. The laser intensity is 10^{13} W/cm^2.

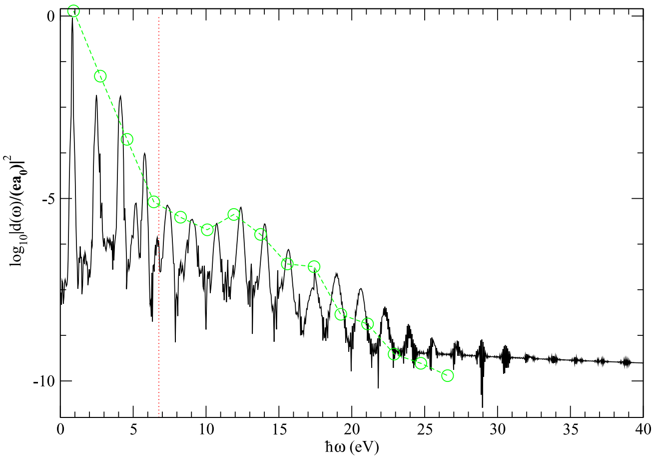

FIG. 2. The HHG power spectra of a Nb atom in a linearly polarized 1500 nm (black solid) and 1353 nm (green) calculated with the TDDFT method. The laser intensity is 10^{13} W/cm^2. The I_p is represented by the vertical dotted red line.

the odd harmonics as green circles. With a slightly higher photon energy, the shifts of the excited states are lowered while the photon energy of the harmonics is increased and the resonances no longer exist. Therefore, H1 (0.916 eV), H3 (2.75 eV), H5 (4.58 eV), and H7 (6.41 eV) essentially follow the linear decay relation. The comparison shows that the five-photon resonance is quite narrow.

The ionization threshold may shift up by the amount of the ponderomotive energy as well. The effective I_p thus becomes 8.9 eV in the 1500-nm laser and 8.5 eV in the 1353-nm laser of 10^{13} W/cm^2. The HHG in these two pulses follow a consistent theme in which a minimum occurs at around 10 eV. Beyond the ionization threshold, ionization is a competitive process to HHG. Ionization could contribute to this minimum. There is an apparent enhancement at around 12 eV, which we interpret as due to a resonance with excited states of the ion. This interpretation is based on the following numerical analysis.

First, we calculate the time profile $d_{\omega=12\,\mathrm{eV}}(t)$ via wavelet transformation [22] of $d(t)$. Consistent with a tunneling ionization, propagation, and recombination picture, it gives two peaks per cycle at $t=\tau$ and $t=\tau+T/2$, where τ is a recombination time and T is the optical cycle. However, values of $d_{\omega=12\,\mathrm{eV}}(t)$ at other times than τ and $\tau+T/2$ are still significant. They are lower than the peak values by only 23% the most. Considering that the kinetic energy accumulated by propagation of the free electron is not the right amount for 12 eV of photon energy release, there must be alternative mechanisms at other times. To identify the routes, we break down the expression of $d(\omega)$ in terms of the field-free electron configurations using the following derivation.

Numerically solving the TDDFT equations gives us the set of time-dependent orbitals in Eq. (4), and

$$\psi_i(\mathbf{r},t)=\sum_j \phi_j(\mathbf{r})c_{ji}(t), \tag{13}$$

where ϕ_j is a field-free orbital with j being the combined spin-orbital index. The summation includes the ground state, excited states, and continuum states.

The dipole moment is a one-electron operator, and its expectation value can be written as the sum of the contributions of the molecular orbitals of the spin orbitals in Slater determinant of Eq. (4). Therefore, for the purpose of analyzing the contributions to the dipole moment, we write the wave function as an orbital product, rather than a Slater determinant:

$$\widetilde{\Psi}(\boldsymbol{r},t)=\prod_{i=1}^{41}\psi_i(\mathbf{r},t). \tag{14}$$

Initially $\widetilde{\Psi}(\boldsymbol{r},0)=\prod_{i=1}^{41}\phi_i(\mathbf{r})$. The time-dependent function $\widetilde{\Psi}(\boldsymbol{r},t)$ defined in Eq. (14) and $\Psi(\boldsymbol{r},t)$ in Eq. (4) include the single-electron, two-electron,..., 41-electron excitations.

The field-induced dipole is

$$\begin{aligned} d(t)&=\langle\tilde{\Psi}(\boldsymbol{r},t)|\hat{z}|\tilde{\Psi}(\boldsymbol{r},t)\rangle\\ &=\sum_{\{j'\}\{j\}}C^*_{\{j'\}}(t)C_{\{j\}}(t)z_{\{j'\}\{j\}}, \end{aligned} \tag{15}$$

where $\hat{z}$ is the $z-$ component of the dipole operator, $\{j\}$ is a collection of 41 indexes, $j_1, j_2, ..., j_{41}$, and

$$C_{\{j\}}(t)=c_{j_1 1}(t)c_{j_2 2}(t)\dots c_{j_{41}41}(t), \tag{16}$$

which is the time-dependent coefficient of an electronic configuration $\{j\}$. The transition dipole element between two configurations $\{j\}$ and $\{j'\}$ is

$$z_{\{j'\}\{j\}}=\langle\phi_{j'_1}\dots\phi_{j'_{41}}|\hat{z}|\phi_{j_1}\dots\phi_{j_{41}}\rangle, \tag{17}$$

where

$$\hat{z}=-e\sum_{i=1}^{41}\hat{z}_i. \tag{18}$$

In this format the Fourier transform of the transient dipole moment is

$$d(\omega)=\sum_{\{j'\}\{j\}}z_{\{j'\}\{j\}}D_{\{j'\}\{j\}}(\omega), \tag{19}$$

where

$$D_{\{j'\}\{j\}}(\omega)=\frac{1}{t_f-t_i}\int_{t_i}^{t_f}C^*_{\{j'\}}(t)C_{\{j\}}(t)e^{-i\omega t}dt. \tag{20}$$

Equation (19) allows us to identify the pairs of configurations $\{j\}$ and $\{j'\}$ that make the largest contribution to $d(\omega)$. The dipole moment matrix element z is zero unless $\{j\}$ and $\{j'\}$ differ by one electron, and the dipole selection rule applies. While z does not depend on either ω or the field, the D elements do. The phases of $C_{j'}$ and C_j have to differ by an amount that is close to ωt. In other words, the shifted energies of the configurations $\{j'\}$ and $\{j\}$ differ by $\sim\hbar\omega$, which limits $\{j\}$ to be the ground-state configuration [Kr]4$d^4$5s. As expected the only significant contribution to $d(\omega=12\,\mathrm{eV}/\hbar)$ comes from the configuration [Kr]4d^4k in combination with the ground state [Kr]4$d^4$5s, where k is a p-wave free-electron orbital. It is consistent with a radiative single-electron recombination from a free-electron state with energy $\epsilon_k=\frac{\hbar^2k^2}{2m_e}$ to the ground state with energy $\epsilon_j=-I_p$ giving $\hbar\omega=\epsilon_k-(-I_p)=\frac{\hbar^2k^2}{2m_e}+I_p$=12 eV.

The enhancement of this harmonic emission points to large magnitudes of $D_{\{[Kr]4d^4k\}\{[Kr]4d^45s\}}(\omega)$, which in turn is

TABLE II. Calculated orbital energy differences ($\Delta\epsilon$) in eV of Nb$^+$ compared to the measured excitation energies $\Delta\epsilon_{\text{exp}}$ from Ref. [28]. The contributions are given in % of the dominant one-electron excitation relative to the ground-state configuration of the ion with $M_L = 2$.

Ionic level	Configuration	I_p	$\Delta\epsilon_{\text{exp}}$	Orbital excitation	Contribution	$\Delta\epsilon$
$^5F_5$	$4d^3(^4F)5s$	7.137	0.356	$4d_0 \rightarrow 5s$	100%	0.709
$^5G_6^\circ$	$4d^3(^4F)5p$	11.069	4.288	$4d_{\pm1} \rightarrow 5p_{\pm1}$	36%	4.604
				$4d_0 \rightarrow 5p_0$	43%	4.393
				$4d_{-1}, 4d_0 \rightarrow 4d_{-2}, 5p_1$	21%	4.250
$^5F_5^\circ$	$4d^3(^4F)5p$	11.366	4.585	$4d_{\pm1} \rightarrow 5p_{\pm1}$	50%	4.604
				$4d_0 \rightarrow 5p_0$	33%	4.393
$^5D_4^\circ$	$4d^3(^4F)5p$	11.431	4.650	$4d_{\pm1} \rightarrow 5p_{\pm1}$	74%	4.604
				$4d_0 \rightarrow 5p_0$	24%	4.393
				$4d_{-1}, 4d_0 \rightarrow 4d_{-2}, 5p_1$	2%	4.250
$^5D_4^\circ$	$4d^3(^4P)5p$	12.187	5.406	$4d_{-1}, 4d_0 \rightarrow 4d_{-2}, 5p_1$	60%	4.250
				$4d_1 \rightarrow 5p_1$	40%	4.604
Average			**4.732**	$4d \rightarrow 5p$		**4.472**
$^5G_6^\circ$	$4d^2(^3F)5s5p(^3P^\circ)$	12.721	5.940			
$^5F_5^\circ$	$4d^2(^3F)5s5p(^3P^\circ)$	12.977	6.196			
$^5D_4^\circ$	$4d^2(^3F)5s5p(^3P^\circ)$	13.264	6.483			
$^5D_4^\circ$	$4d^2(^3P)5s5p(^3P^\circ)$	13.972	7.191			

connected to large values of $|C_{\{[Kr]4d^4k\}}(t)|$ [Eq. (20)] or a significant population in [Kr]$4d^4k$. In principle, a photon-free resonance may populate this configuration if it couples to other populated configurations of similar energy. To verify this, we compute and search for two-electron excited configurations $\{j'\}$ such that $|D_{\{j'\}\{[Kr]4d^45s\}}(\omega = 12\,\text{eV}/\hbar)| > 10^{-7}$. Note that $|D_{\{[Kr]4d^4k\}\{[Kr]4d^45s\}}(\omega)|$ is in the order of 10^{-6}.

It turns out that both [Kr]$4d^35p_0k_1$ and [Kr]$4d^35p_{\pm1}k_2$, where k_1 and k_2 each stands for an s-wave free-electron wave function, render a $|D(\omega)|$ value that is higher by two orders of magnitude than $|D_{\{[Kr]4d^4k_3\}\{[Kr]4d^45s\}}(\omega)|$. Both $[Kr]4d^35p_0k_1$ and $[Kr]4d^35p_{\pm1}k_2$ are coupled to $[Kr]4d^4k_3$ via exchange. It is the coupling between the configuration of an excited ion with a lower energy electron and a ground-state ion with a high-energy electron.

Limited by the adiabatic approximation of the time-dependent exchange-correlation potential, such coupling at time t will not be included if the population of $[Kr]4d^35p_0k_1$ or $[Kr]4d^35p_{\pm1}k_2$ only spikes at a particular time $t' \neq t$. The reason for our calculation to render an enhanced HHG emission at ∼12 eV via resonance with an ion excited state is a constant significant population of the ion excited state, which is created in multiple channels. Some of them are ionization from the configuration $[Kr]4d^35s5p_{0,\pm1}$ created by either excitation of the neutral atom or coupling to $[Kr]4d^45p_0$ or other configurations of the neutral atom. Other channels include excitations of the ground-state ionic configuration with various kinetic energies of the free electron. Excitation of the neutral atom is particularly enhanced in the 1500-nm laser. Excitation of the cation takes more energy and the energies of the excited states of Nb$^+$ are given in Table II. The AC Stark shift of a cation is insignificant due to the positive charge.

The intensity of the incident laser determines the Stark shifts and hence it impacts the resonances. In Fig. 3 we plot the calculated HHG spectra in the linearly polarized 1500-nm lasers of 1, 2, and 3×10^{13} W/cm^2 with the same pulse length of 20 optical cycles. They are as expected for most harmonics: The intensity of a harmonic emission increases in a stronger field, i.e., it is the largest in the 3×10^{13} W/cm^2 laser and lowest in the 10^{13} W/cm^2 laser. The few exceptions, however, demonstrate how the perceived resonances are influenced by the intensity of the incident light, and hence shine some light on the Stark shifts, including those for the ionization threshold.

One of the obvious exceptions is H5, for which the harmonic intensity is the largest in the 10^{13} W/cm^2 pulse. This supports our interpretation that the excitation energy for $4d \rightarrow 5p$ is shifted to be 4 eV in the 10^{13} W/cm^2 laser and is substantially larger in more intense lasers. At 5.78 eV H7 in the 1 and 2×10^{13} W/cm^2 lasers shares an almost identical intensity, while in 3×10^{13} W/cm^2 it is only slightly more intense. Apparently, factors other than the field strength are at play which enhance H7 in the 10^{13} W/cm^2 laser. Most likely

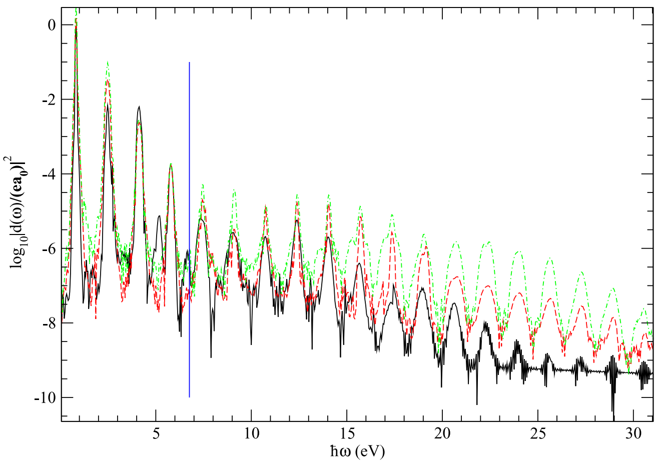

FIG. 3. The HHG of a Nb atom in a linearly polarized 1500-nm pulsed laser calculated with the TDDFT method. The laser intensity is 1 (black solid), 2 (red), and 3 (green) $\times 10^{13}$ W/cm^2, respectively. The I_p is represented by the vertical solid blue line.

the five-photon resonance with the $4d \rightarrow 5p$ excitation also enhances H7.

In the strongest field, H11 (at 9.11 eV) appears to be particularly enhanced. We consider this as 11-photon resonance with the much shifted excited state $x^6D^\circ_{9/2}$. In the 2×10^{13} and 3×10^{13} W/cm^2 lasers, H13 (at 10.7 eV) shares a similar intensity, indicating an enhancement for the former.

We use Eq. (19) to analyze the enhancement of H13 in the 2×10^{13} W/cm^2 pulse. The source of H13 is found to be radiative transitions from the Rydberg state configurations [Kr]$4d^4np_0$, where $n = 7$–10, to the ground state. For a Rydberg orbital np_0 with $n = 7, 8, 9, 10$, more than 90% of the electron density is distributed between 10 a_0 and 100 a_0 from the core. When $n_1 = 7$, the last node is at 17 a_0 and the furthest peak is at 26 a_0. In the 2×10^{13} W/cm^2 pulse the Rydberg states may shift up by as much as the ponderomotive energy of 4.2 eV, which makes them higher than the ground state by 10.7 eV, the photon energy of H13.

We search for other excited configurations that influence the populations of [Kr]$4d^4np_0$ by scanning the largest magnitudes among the elements of $D(\omega = 10.7\,\mathrm{eV}/\hbar)$, which are defined in Eq. (20). We find that they belong to the combination of the ground-state configuration and one of the following excited configurations: [Kr]$4d^4n_0s$, where $n_0 = 7$–11; [Kr]$4d^35sn_1d$, where $n_1 = 8$–10; and [Kr]$4d^35p_{\pm1}n_2s$, where $n_2 = 16 - 24$. Rydberg states [Kr]$4d^4n_0s$ and [Kr]$4d^35sn_1d$ both couple to [Kr]$4d^4np_0$ by the dipole operator. Such couplings are not associated with any photon absorption or emission because their energy differences are too small.

Noticeably, [Kr]$4d^4n_0s$ and [Kr]$4d^35p_{\pm1}n_2s$ share similar energies even though $n_2 > n_0$. The reason is that the shift of the latter is much smaller. For n_2s, $n_2 = 16, \ldots, 24$, at least 93% of the electron population is more than 100 a_0 from the core, and the radial probability density distributions do not decrease at large distances. We therefore consider consider n_2s as free-electron orbitals and [Kr]$4d^35p_{\pm1}n_2s$ as excited configurations of Nb$^+$, abbreviated as $4d^35p$. Listed in Table II are some ion excited states with the configuration $4d^35p$ whose energy are closed to 10.7 eV. Configurations [Kr]$4d^35p_{\pm1}n_2s$ and [Kr]$4d^4n_1p_0$ couple by exchange. This is the resonance between the excited states of a cation and the high Rydberg states of the neutral species.

IV. SUMMARY AND CONCLUSIONS

Using a TDDFT method, we study the many-electron dynamics in the HHG of niobium. The computed orbital energies are consistent with the average of the measured excitation energies. The $5s$ orbital contributes the most to the induced dipole. However, the resonance-enhanced HHG in the 1500-nm lasers mostly involves the $4d \leftrightarrow 5p$ transition. Comparing the HHG spectra of Nb in lasers of different intensities, we confirm that the excitation energies of the neutral atom increase with the laser intensity. The electron that initially occupies the $5s$ orbital moves farther away from the core as the laser intensity increases, which causes the $4d$ orbital to be more bound. Meanwhile the energies of the Rydberg states increase. The combined effect causes the enhanced peaks shift to higher energies, and the amount of shift is close to the quivering energy of a free electron.

Above the I_p, enhanced HHG occurs at ∼11–13 eV, which are the energies of the ion excited states with configuration $4d^35p$. The enhancement at ∼11 eV is particularly prominent when the laser intensity is 2×10^{13} W/cm^2. At this intensity, a near-threshold Rydberg state of Nb with the configuration $4d^4\,np$, where $n > 5$, is in resonance with a $4d^35p$ ionic state.

The numerical modeling and analysis presented in this work demonstrate how the many-electron dynamics impact the strong-field processes. The Rydberg states of Nb with the configuration $4d^35s\,np$ causes enhanced HHG below the I_p in certain IR lights. Since the $5s$ orbital is the most active, a $4d^35s\,np$ excited state cannot be reached with a SAE in strong field. The energy of the excited states increases linearly with laser intensity, which is reflected in the shifts of the enhanced HHG peaks as well as in the elevated ionization threshold which reduces ionization probability. Many-electron dynamics also creates and transforms resonances between the neutral and the cation, which leads to enhanced HHG or ionization.

ACKNOWLEDGMENTS

This work is supported by National Science Foundation Grant No. PHY-1506441 and used the Extreme Science and Engineering Discovery Environment (XSEDE) expanse compute cluster at the San Diego Supercomputer Center at UC San Diego through Grant No. TG-PHY210099.

---

[1] N. Saito, N. Ishii, T. Kanai, S. Watanabe, and J. Itatani, Sci. Rep. **6**, 35594 (2016).

[2] T. Gaumnitz, A. Jain, and H. J. Wörner, Opt. Express. **26**, 14719 (2018).

[3] B. Wolter, M. G. Pullen, A. T. Le, M. Baudisch, K. Doblhoff-Dier, A. Senftleben, M. Hemmer, C. D. Schroeter, J. Ullrich, T. Pfeifer *et al.*, Science **354**, 308 (2016).

[4] S. Tochitsky, E. Welch, M. Polyanskiy, I. Pogorelsky, P. Panagiotopoulos, M. Kolesik, E. M. Wright, S. W. Koch, J. V. Moloney, J. Pigeon *et al.*, Nat. Photonics **13**, 41 (2019).

[5] D. R. Austin, A. S. Johnson, F. McGrath, A. D. Wood, L. Miseikis, T. Siegel, P. Hawkins, A. Harvey, Z. Mašín, S. Patchkovskii *et al.*, Sci. Rep. **11**, 2485 (2021).

[6] K. J. Schafer, B. Yang, L. F. DiMauro, and K. C. Kulander, Phys. Rev. Lett. **70**, 1599 (1993).

[7] P. B. Corkum, Phys. Rev. Lett. **71**, 1994 (1993).

[8] M. Meckel, D. Comtois, D. Zeidler, A. Staudte, D. Pavicic, H. C. Bandulet, H. Pepin, J. C. Kieffer, R. Doerner, D. M. Villeneuve *et al.*, Science **320**, 1478 (2008).

[9] A. J. Uzan, H. Soifer, O. Pedatzur, A. Clergerie, S. Larroque, B. D. Bruner, B. Pons, M. Ivanov, O. Smirnova, and N. Dudovich, Nat. Photonics **14**, 188 (2020).

[10] S.-J. Wang, J. Danek, C. I. Blaga, L. F. DiMauro, J. Biegert, and C. D. Lin, J. Chem. Phys. **155**, 164104 (2021).

[11] X. Liu, K. Amini, A. Sanchez, B. Belsa, T. Steinle, and J. Biegert, Commun. Chem. **4**, 154 (2021).

[12] M. Kübel, Z. Dube, A. Y. Naumov, D. M. Villeneuve, P. B. Corkum, and A. Staudte, Nat. Commun. **10**, 1042 (2019).
[13] P. C. Li, Y. L. Sheu, C. Laughlin, and S. I. Chu, Nat. Commun. **6**, 7178 (2015).
[14] P. Li, Y. L. Sheu, H. Z. Jooya, X. X. Zhou, and S. I. Chu, Sci. Rep. **6**, 32763 (2016).
[15] N. B. Delone and V. P. Krainov, Phys. Usp. **42**, 669 (1999).
[16] S. Bengtsson, E. Larsen, D. Kroon, S. Camp, M. Miranda, C. Arnold, A. LHuillier *et al.*, Nat. Photonics **11**, 252 (2017).
[17] E. R. Simpson, M. Labeye, S. Camp, N. Ibrakovic, S. Bengtsson, A. Olofsson, K. J. Schafer, M. B. Gaarde, and J. Mauritsson, Phys. Rev. A **100**, 023403 (2019).
[18] X. Chu and S.-I Chu, Phys. Rev. A **70**, 061402(R) (2004).
[19] X. Chu and G. C. Groenenboom, Phys. Rev. A **94**, 053417 (2016).
[20] O. Smirnova, Y. Mairesse, S. Patchkovskii, N. Dudovich, D. Villeneuve, P. Corkum, and M. Y. Ivanov, Nature (London) **460**, 972 (2009).
[21] H. Wörner, J. Bertrand, D. Kartashov, P. Corkum, and D. Villeneuve, Nature (London) **466**, 604 (2010).
[22] X. Chu and G. C. Groenenboom, Phys. Rev. A **87**, 013434 (2013).
[23] M. Smits, C. A. de Lange, A. Stolow, and D. M. Rayner, Phys. Rev. Lett. **93**, 213003 (2004).
[24] E. Murakami, R. Mizoguchi, Y. Yoshida, A. Kitashoji, N. Nakashima, and T. Yatsuhashi, J. Photochem. Photobiol. A **369**, 16 (2019).
[25] X. Chu and G. C. Groenenboom, Phys. Rev. A **96**, 013421 (2017).
[26] X. Chu and G. C. Groenenboom, Phys. Rev. A **101**, 043423 (2020).
[27] X.-M. Tong and S.-I. Chu, Phys. Rev. A **57**, 452 (1998).
[28] A. Kramida, Yu. Ralchenko, J. Reader, and NISTASDTeam, NIST Atomic Spectra Database (Version 5.3) (National Institute of Standards and Technology, Gaithersburg, 2015), http://physics.nist.gov/asd.
[29] R. N. Zare, *Angular Momentum* (Wiley, New York, 1988).